# PAPER 137 – COMPUTATIONAL DEVELOPMENT AND AERODYNAMIC ANALYSIS OF A SINGLE-STAGE LAUNCH VEHICLE TO SUBDUE POST-LAUNCH RISK

A. Jinadu[1*], A. M. Oluwatofunmi[1], O. A. Olayemi[1], T. Dmytro[2], V. Koloskov[3]

[1]Department of Aeronautical and Astronautical Engineering, Faculty of Engineering, Kwara State University, Kwara State, Nigeria.
[2]Nanjing University of Aeronautics and Astronautics, Nanjing, China.
[3]National University of Civil Defence of Ukraine, Ukraine.
[*]Email: abdulbaqi.jinadu@kwasu.edu.ng

***ABSTRACT***
The aerospace industry has prioritized reducing fatalities and failure rates after the launch of a vehicle resulting from system or engine failure. Rocketry has been difficult over the years, and international players in the industry are constantly attempting to learn from any failures. This paper aims to decrease material, resource, and payload waste while ensuring crew safety by focusing on the computational modelling and aerodynamic analysis of a single-stage launch vehicle. CATIA V5 was utilized to create the computational model of a triggered nose cone rocket booster while ANSYS was used to analyse the trigger nose cone at different angles of attack and determine how the trigger nose cone will behave in case of emergencies such as system or engine failure, which could lead to the complete explosion of the launch vehicle. Based on the current findings, the trigger nose cone is not in the safe zone when ejected at an angle of attack greater than 20° due to the shockwave's effect on its surface when ejected from the main body of the launch vehicle.

***KEYWORDS***: Post-launch, Engine failure, Single-stage launch vehicle, Trigger nose cone, Combustion chamber.

## 1. INTRODUCTION

The mission of humans and payloads to space, though quite involving, has been a success story in the recent and distant past. In earlier years, there was little need for such skills in spaceflight. This changed dramatically in 1986 with the loss of the Space Shuttle Challenger and was perpetuated by the loss of Space Shuttle Columbia in 2003 (Banks et. Al 2019). However, a lot of failures in the journey of man and payload to space via launch vehicles, space shuttles, and spaceships, has been recorded in the past which have resulted in fatalities of the crew and other things on board, wastage of resources, time, and capital spent on building each of the launch vehicles that failed. Comparing the costs of different launch vehicles, the possibility of the risk of failure is assumed to be accounted for by the cost of insurance (Parkinson, 1999).

According to Chang (1996), The failure of a Launch Vehicle is attributed to associated problems such as structures and propulsion. It was also brought to notice by Gorbenko et al. (2009) in a study of Orbital Carrier Rocket and Spacecraft Failure: 2000-2009 that the probability of fatal and partial spacecraft failure and mechanical damage increased from 0.059 to 0.073.

Karacalioglu & Bukley (2015) cited that some of these failures are due to system failures. Fernández et al. (2022) noted that trajectory and attitude control and the separation systems account for over a 90% of space launch vehicle failures. System failure may occur before, during, or after the launch of any launch vehicle, such as a single-stage, two-stage, or three-stage launch vehicle. Failure could happen during the separation of the nose cone of a single stage to orbit (SSTO) launch vehicle or when each stage detaches itself from the preliminary stage of such a launch vehicle, which could lead to loss of control and navigation of the launch vehicle by the ground station or astronaut on board. In a time in which a significant number of launch vehicles are being developed, boosted by numerous new space actors demanding cheaper access to space, the need to ensure the reliability of launch vehicles and the performance of a successful Post-Mission Disposal (PMD) is undeniable (Fernández et al. 2022).

Furthermore, failures as a result of human error, such as with Electron Szondy, (2017), Falcon 9 etc., may occur during the preliminary stage of the launch vehicle's design, which may not only lead to the launch vehicle's failure but also affect things present on board such a launch. Wrong input of data by the ground station can also lead to the failure of the launch vehicle, which may lead to the malfunction of the launch vehicle's peripheral systems such as the propulsion system, control system, and re-entry system, which could jeopardize the survivability of the crew on board.

Other failures, such as Astra's Launch Vehicle 0010 and Rocket Lab (2021) may be due to engine malfunction. Such a failure makes it impossible for the launch vehicle to be successful in its mission. This failure may lead to the failure of the propulsion system because of the failure in the combustion process and cycle that occur between LOX (liquid oxygen) and LH2 (liquid hydrogen) or kerosene or any kind of liquid fuel-based combustion system,

or because of the failure that occurs in the ignition process of the solid fuel system, which leaves no space for the crew and things present on board to escape from such a launch vehicle.
On Analysis of Space Launch Vehicle Failures and Post Mission Disposal Statistics, most of these failures are not limited to but mostly occur within the propulsion, separation, trajectory and, attitude control systems (Ayala et al., 2022). Based on the conclusion of the research, these three subsystems alone account for 90% of launch failures, with 54% corresponding to the propulsion system. Mathematical model approach has helped to improve the level of safety (Melnikov & Davydova 2018).

## 4. THEORETICAL ANALYSIS

### 2.1 Six Degrees of freedom (6DOF) solver theory

The six-degree of freedom solver in ANSYS Fluent uses the object's forces and moments to compute the translational and angular motion of the center of gravity of an object. The governing equation for the translational motion of the center of gravity is solved in the inertial coordinate system.

$$\dot{\overrightarrow{v_G}} = \frac{1}{m}\sum \overrightarrow{f_G} \tag{1}$$

where $\overrightarrow{v_G}$ is the translational motion of the center of gravity, $m$ is the mass, and $\overrightarrow{f_G}$ is the force vector due to gravity. The angular motion of the object, $\dot{\overrightarrow{\omega_B}}$, is more easily computed using body coordinates:

$$\dot{\overrightarrow{\omega_B}} = L^{-1}\left(\sum \overrightarrow{M_B} - \overrightarrow{\omega_B} \times L\overrightarrow{\omega_B}\right) \tag{2}$$

where L is the inertia tensor, $\overrightarrow{M_B}$ is the moment vector of the body, and $\overrightarrow{\omega_B}$ is the rigid body angular velocity vector. The moments are transformed from inertial to body coordinates using equation (3)

$$\overrightarrow{M_B} = R\overrightarrow{M_G} \tag{3}$$

where R represents the following transformation matrix:

$$\begin{matrix} C_\theta C_\varphi & C_\theta C_\varphi & -S_\theta \\ S_\emptyset S_\theta C_\varphi - C_\emptyset S_\varphi & S_\emptyset S_\theta S_\varphi + C_\emptyset C_\varphi & S_\emptyset C_\theta \\ C_\emptyset S_\theta C_\varphi + S_\emptyset S_\varphi & C_\emptyset S_\theta C_\varphi - S_\emptyset C_\varphi & S_\emptyset C_\theta \end{matrix} \tag{4}$$

where in generic terms, $C_x = \cos(x)$ *and* $S_x = \sin(x)$. The angles $\emptyset, \theta$ *and* $\varphi$ are Euler angles.
The angular and translational velocities are used in the dynamic mesh calculations to update the rigid body position (Ahamed et al., 2014).

### 2.2 Rocket Equation

The change in mass of launch vehicle as it accelerates is given by Equation (5) (Lepsch Jr et al., 1995).

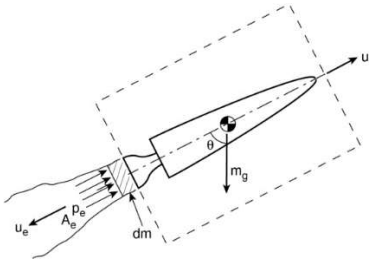


Fig 1. Schematic for application of the momentum theorem (Tartabini et al., 2015)

As shown in Figure 1, by considering a small mass, $dm$, expelled from the trigger nose cone during time $dt$, the initial momentum of the mass in the control volume is, $m$-$v.du$. The final momentum of mass in the control volume is

$$(M_v - dm)(u + du) + (u - u_e)dm = m_v u + m_v du - udm - dudm + udm - u_e dm \tag{5}$$

The change in momentum during the interval $dt$ is

$$\text{momentum}_{\text{final}} - \text{momentum}_{\text{initial}} = m_v du - u_e du \quad (6)$$

The net force acting on the system is given by Equation (7)

$$\sum F = (p_e - p_o)A_e - D - mg\cos\theta. \quad (7)$$

Applying conservation of momentum, the resulting impulse, $\sum Fdt$, must balance the change in momentum of the system:

$$m_v du - dmu_e = \left[(p_e - p_o)A_e - D - m_v g\cos\theta\right]dt \quad (8)$$

Then since

$$dm = \dot{m}dt = -\frac{dm_v}{dt}dt, \quad (9)$$

where $\dot{m}$ is the propellant mass flow rate, the equation reads:

$$m_v du = \left[(p_e - p_o)A_e + \dot{m}u_e - D - m_v g\cos\theta\right]dt \quad (10)$$

For $p_e = p_o$,

$$du = -\frac{u_e dm_v}{m_v} - \frac{D}{m_v}dt - g\cos\theta dt \quad (11)$$

Eq. (11) is known as the Rocket/launch vehicle Equation. It can be integrated as a function of time to determine the velocity of the rocket/launch vehicle.

If $u_e = constant$, assuming that at $t = 0, u = 0$, neglecting drag, and assuming $\theta = 0$, then the rocket equation can be simplified as

$$du = -u_e\frac{dm_v}{m_v} - gdt, \quad (12)$$

which can be integrated to give

$$u = -u_e In\left(\frac{m_v}{m_{vo}}\right) - gt, \quad (13)$$

where $m_{vo}$ is the initial mass of the rocket/launch vehicle. Equation (12) can be re-written as

$$u = g\left[In\left(\frac{m_v}{m_{vo}}\right) - t\right], \quad (14)$$

This equation (14) can be likened to the Breguet Range Equation for aircraft. It shows the overall dependence of the primary performance parameter for a rocket (velocity, $u$) on propulsion system efficiency (Isp) and structural design.

Assuming the rate of fuel consumption is constant, the mass of the rocket or launch vehicle varies over time as

$$m_v(t) = m_{vo} - (m_{vo} - m_{v,final})\frac{t}{t_b} \quad (15)$$

where $t_b$ is the time at which all propellants are used. This expression can be substituted into the equation for velocity and then integrated to find the height at the end of burnout:

$$h_b = \int_0^{t_b} u dt, \quad (16)$$

which for a single-stage sounding rocket with no drag and constant gravity yields

$$h_b = g\left[-t_b Isp\frac{In\left(\frac{m_{vo}}{m_{v,final}}\right)}{\left(\frac{m_{vo}}{m_{v,final}} - 1\right)} + t_b Isp - \frac{1}{2}{t_b}^2\right] \quad (17)$$

The final height of the rocket can then be determined by equating the kinetic energy of the vehicle at burnout with its change in potential energy between that point and the maximum height.

## 5. MATERIALS AND METHODS

The computational setup for the aerodynamics analysis in this experiment was carried out using Ansys Fluid Fluent. Given the fluidic nature of the analysis, a suitable computational domain was constructed to ensure accurate results. The adopted computational domain, mesh, and boundary conditions are illustrated in figure 2 below.

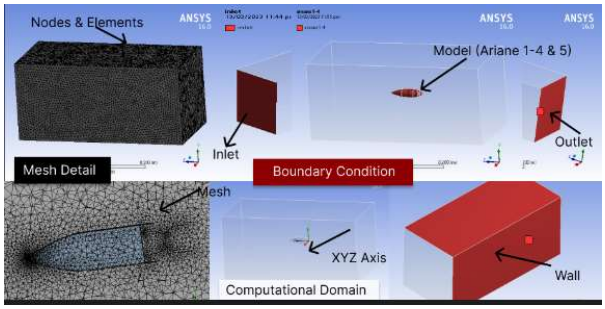


Fig 2: Computational domain, mesh and boundary condition (Author).

The computational domain was constructed in the form of a wedge geometry, representing a 14.940° section of the corresponding 3D domain. The property volume of the computational model is 0.1642 $m^3$, with a bounding box measuring 0.225 m in length on the X and Y axis and 0.48753 m in length on the Z axis.
To ensure reliable results, a uniform computational mesh was used. The Ariane 5 prototype's mesh consists of 29,299 triangular nodes and 160,880 elements. The Ariane 1-4 series prototype's mesh consists of 92,207 triangular nodes and 374,333 elements.
This made it possible to accurately analyze the aerodynamics of the prototypes under consideration. In addition, the initial conditions used for the validation case were summarized in Table 1, providing a comprehensive overview of the experimental conditions and results.

Table 1: Input Parameters (validation case)

| Parameter | Value | Units |
|---|---|---|
| **Fluid Density** | 1.225 | $Kg/m^3$ |
| **Temperature** | 288.16 | K |
| **Viscosity** | 1.7894e-05 | $Kg/m^{-s}$ |
| **Specific Heats Ratio** | 1.4 | - |

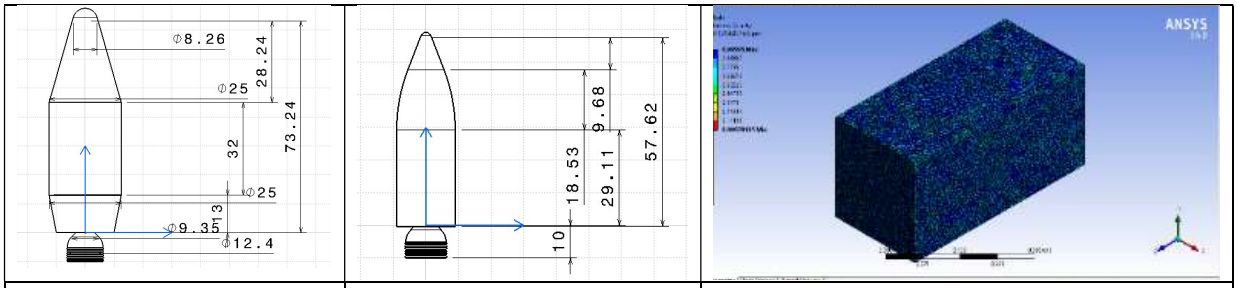


(a) Ariane 1-4 | (b) Ariane 5 series | (c) Rectangular mesh enclosure of model.

Fig 3(a-c): Schematic diagram of Ariane 1-4 and Ariane 5 series and the mesh of a rectangular enclosure around the trigger nose cone model on ANSYS (Author)

The schematic diagram of the models and its rectangular mesh are seen in Figure 3(a-c) above. The tank, nozzle system, combustion system, and trigger nose cone were modeled using CATIA. The choice of CATIA was based on its interface, which supports computational modeling, while Ansys was used for Computational Aerodynamics analysis, as it has a suitable interface for this purpose. Figure 4 shows the meshing and boundary conditions applied using ANSYS Fluid Flow (Fluent).

## 6. RESULTS AND DISCUSSION

The stress impact of air velocity at Mach 0.6 is shown in figure 4(a-n) after some simulations of the proposed CAD models using the ANSYS CFD FLUENT workbench to carry out the aerodynamics analysis of the model to know how they react at different angles of attack.

### 4.1 Fluid Flow Fluent

When a trigger nose cone is discharged from a launch vehicle for an emergency case, the effect of drag force is plotted using the ANSYS Fluid Fluent. Its response to its surrounding medium while ejecting and re-landing in a secure environment at Mach 0.6 will be observed from various angles of attack.

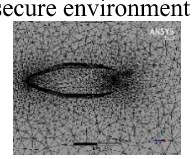

a) (Ariane 1-4 series) at 0º angle of attack

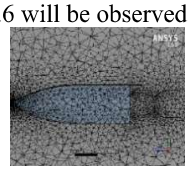

(b) (Ariane 5) at 0º angle of attack

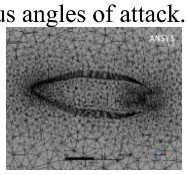

c) (Ariane 1-4 series) at 5º angle of attack

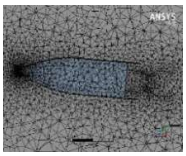

d) (Ariane 5) at 5º angle of attack

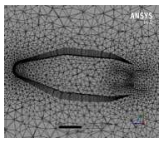

e) (Ariane 1-4 series) at 10º angle of attack

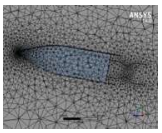

(f) (Ariane 5) at 10º angle of attack

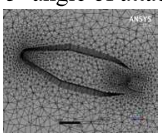

g) (Ariane 1-4 series) at 15º angle of attack

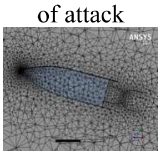

(h) (Ariane 5) at 15º angle of attack

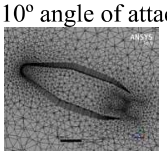

i) (Ariane 1-4 series) at 20º angle of attack

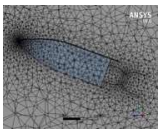

(j) (Ariane 5) at 20º angle of attack

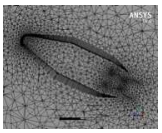

k) (Ariane 1-4 series) at 25º angle of attack

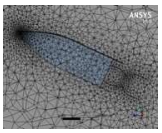

(l) (Ariane 5) at 25º angle of attack

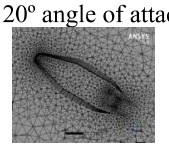

(m) (Ariane 1-4 series) at 30º angle of attack

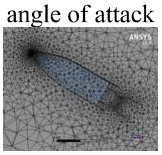

(n) (Ariane 5) at 30º angle of attack

Fig 4(a-n): Mesh cross-section view of trigger nose cone at various angles of attacks (Author)

It is observed that the convergence history of Ariane 1-4 differs from that of current study (Ariane 5). This shows that the stability of the trigger nose cone at different angles of attack varies based on its shape. It is also observed that each model tends to be unstable at the first stage of being ejected from the main body of the launch vehicle due to the viscous and pressure forces generated as each component tends to interact with their immediate environment.

Table 2 The Viscous and Pressure Convergence History for Trigger Nose Cone of current study (Ariane 5)

| Angle of Attack (º) | Viscous (Pa. s) | Pressure (Pa) | Angle of Attack (º) | Viscous (Pa. s) | Coefficient of Pressure |
|---|---|---|---|---|---|
| 0 | 0.000173489 | -0.032071135 | 0 | 0.000283247 | -0.052361361 |
| 5 | -0.000199944 | 0.029084287 | 5 | -0.000326438 | 0.047484551 |
| 10 | -0.000199944 | 0.029084287 | 10 | -0.000326438 | 0.047484551 |
| 15 | -0.00118218 | 0.068081288 | 15 | -0.001719448 | 0.11115312 |

| | | | | | |
|---|---|---|---|---|---|
| 20 | 0.000913956 | 0.046168723 | 20 | 0.001492172 | 0.075377506 |
| 25 | 0.000347398 | 0.016404732 | 25 | 0.000567181 | 0.026783236 |
| 30 | 0.000347398 | 0.016404732 | 30 | 0.000567181 | 0.026783236 |

Table 3 The Viscous and Pressure Convergence History for Trigger Nose Cone (Ariane 1-4 series)

| Angle of Attack (°) | Viscous (Pa. s) | Pressure (Pa) | Angle of Attack (°) | Viscous (Pa. s) | Coefficient of Pressure |
|---|---|---|---|---|---|
| 0 | 0.00017348892 | -0.032071135 | 0 | 0.00028324722 | -0.052361037 |
| 5 | -0.00019994352 | 0.029084287 | 5 | -0.0003264384 | 0.047484551 |
| 10 | -0.00019994352 | 0.029084287 | 10 | -0.0003264384 | 0.047484551 |
| 15 | -0.0011021804 | 0.068081288 | 15 | -0.0017994782 | 0.11115312 |
| 20 | 0.0011727725 | 0.051545741 | 20 | 0.000191966 | 0.084156311 |
| 25 | 0.0024728612 | 0.032727325 | 25 | 0.0040373245 | 0.053432368 |
| 30 | -0.0006705494 | -0.087020394 | 30 | -0.0010947745 | -0.14207411 |

The values of the viscous and pressure forces tend to differ depending on the angle of attack of the trigger nose cone. As a result, the influence viscosity of the fluid (air), pressure drag, and normal force have on the surface of the nose cone at different angles of attack results in positive and negative values. This positive and negative viscosity indicates the resistivity and the acceleration of each model at different angles of attack as shown in Table 2 and Table 3.

### 4.2 The velocity plane view of a trigger nose cone angle of attack

Based on the computational aerodynamic analysis presented in Figures 5(a-n) below, it can be inferred that, in the Ariane (1-4 series), the effect of shock waves and aerodynamic disturbances is relatively insignificant within the 0-15° angle of attack range when compared to the 20°-30° range. This is observable by the light yellow and green colours in the images below. As a precaution, it is advisable to eject each triggering nose cone within an angle of attack range of 0°-15°. Any angle beyond this range poses a certain degree of risk.

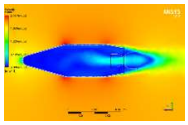

(a) (Ariane 1-4 series) at 0° angle of attack

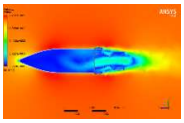

(b) (Ariane 5) at 0° angle of attack

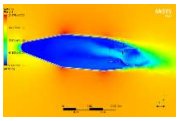

(c) (Ariane 1-4 series) at 5° angle of attack

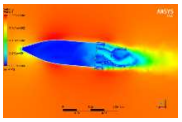

(d) (Ariane 5) at 5° angle of attack

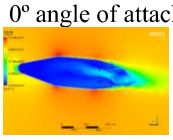

(e) (Ariane 1-4 series) at 10° angle of attack

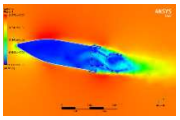

(f) (Ariane 5) at 10° angle of attack

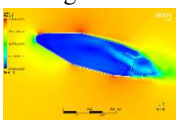

(g) (Ariane 1-4 series) at 15° angle of attack

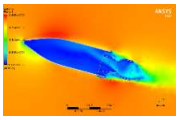

(h) (Ariane 5) at 15° angle of attack

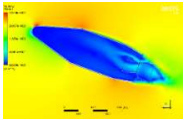

(i) (Ariane 1-4 series) at 20° angle of attack

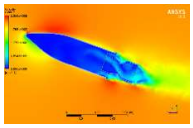

(j) (Ariane 5) at 20° angle of attack

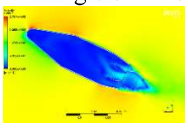

(k) (Ariane 1-4 series) at 25° angle of attack

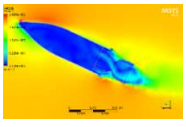

(l) (Ariane 5) at 25° angle of attack

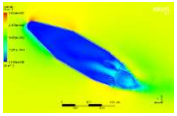

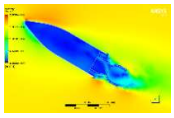

(n) (Ariane 5) at 30° angle of attack

(m) (Ariane 1-4 series) at 30º angle of attack

Fig. 5(a-n). The velocity plane view of trigger nose cone at various angles of attacks (Author).

During the research conducted on the Ariane 5, it was discovered that the impact of shock waves and aerodynamic disturbances was significantly lower within the 0-15º angle of attack range compared to the 20-30º range. As a safety precaution, it is recommended that trigger nose cones be ejected within the 0-15º angle of attack range, which has been determined to be the safest zone for ejection. It is advised to eject the trigger nose cone within a range of 0-15º angle of attack, with a minimum of 0º and a maximum of 15º, to ensure maximum safety.

## 7. CONCLUSION

a. In the range of 0º angle of attack to 30º angle of attack at Mach 0.6, the stability of the trigger nose cone varies based on its shape.
b. It confirms the standard safe zone for each trigger nose cone lies in the range of 0–15º angles of attack.
c. Any zone with an angle of attack greater than 20º is a no-go zone because the shock waves have a larger effect on the surface, which could lead to a loss of control of the trigger nose cone.

## ACKNOWLEDGEMENT

This research was supported by Kwara State University, Malete. Gratitude to Olalekan Adebayo Olayemi and Ayinde Marvelours Oluwatofunmi who provided expertise that greatly assisted the research.
Appreciation to Tiniakov Dmytro and Volodymyr Koloskov for moderating the manuscript.

## REFERENCES

1. Banks, R., Auñón, S. M., Harding, R., & Mumbower, A. (2019). Spacecraft Accident Investigation. Principles of Clinical Medicine for Space Flight, 885-904. https://doi.org/10.1007/978-1-4939-9889-0_30
2. Parkinson, R. C. (1999). The hidden costs of reliability and failure in launch systems. Acta Astronautica, 44(7-12), 419-424. https://doi.org/10.1016/S0094-5765(99)00093-4
3. Chang, I. S. (1996). Investigation of space launch vehicle catastrophic failures. Journal of spacecraft and rockets, 33(2), 198-205. https://doi.org/10.2514/3.26741
4. Gorbenko, A., Kharchenko, V., Tarasyuk, O., & Zasukha, S. (2009). A study of orbital carrier rocket and spacecraft failures :179–198. https://doi.org/10.11610/isij.2815
5. Karacalioglu, A. G., & Bukley, A. (2015). Examining the Underlying Causes of Space Launch Failures. In Space Safety is No Accident: The 7th IAASS Conference (pp. 179-188). Springer International Publishing. https://doi.org/10.1007/978-3-319-15982-9_21
6. Fernández, L. A., Wiedemann, C., & Braun, V. (2022). Analysis of Space Launch Vehicle Failures. In XXVI International Congress 31st August–3rd September 2021 On-line event hosted by the Tuscany AIDAA Section in Pisa. https://doi.org/10.24355/dbbs.084-202202091543-0
7. Fernández, L. A., Wiedemann, C., & Braun, V. (2022). Analysis of Space Launch Vehicle Failures and Post-Mission Disposal Statistics. Aerotecnica Missili & Spazio, 101(3), 243-256. https://doi.org/10.1007/s42496-022-00118-5
8. Szondy, B. D. (2017). Electron rocket failure caused by ground error.
9. Rocket Lab identifies cause of Electron failure. (2021). 2021–2022.
10. Ayala, L. F., Carsten, W. &, Viatli, B. (2022). Analysis of Space Launch Vehicle Failures and Post - Mission Disposal Statistics. Aerotecnica Missili & Spazio, 243-256. https://doi.org/10.1007/s42496-022-00118-5
11. Melnikov, B., & Davydova, E. (2018). Mathematical modeling of increasing the level of safety in case of failures of space technology. International Journal of Open Information Technologies, 6(5), 1-6.
12. https://www.popularmechanics.com/space/rockets/g18751736/rocket-launch-failures/
13. Ahamed, S. N., Kumar, J. V., Mushraffuddin, M., & Shrawini, P. (2014). Modeling And Analysis of

Rocket Outer Shell. International Journal of Scientific & Technology Research, 3(4) 270–280.

14. Lepsch Jr, R. A., Stanley, D. O., & Unal, R. (1995). Dual-Fuel Propulsion in Single-Stage Advanced Manned Launch System Vehicle. NASA Technical Reports Server Journal of Spacecraft and Rockets. 32(3) 417–425. https://doi.org/10.2514/3.26631.
15. Tartabini, P. V., Beaty, J. R., Lepsch, R. A. & Gilbert, M. G. (2015) Payload Performance Analysis for a Reusable Two-Stage-to-Orbit Vehicle. No. NASA/TM-2015-218760.
16. Bussler, L., & Sippel, M. (2017). Comparison of Reusable First Stage Return Options, 21st AIAA International Space Planes and Hypersonics Technologies Conference 1-15. https://doi.org/10.2514/6.2017-2137.